JACS JOURNAL OF THE AMERICAN CHEMICAL SOCIETY

Caltech Library

Subscriber access provided by Caltech Library

Article

EPR spectroscopy of iron- and nickel-doped [ZnAl]-layered double hydroxides: modeling active sites in heterogeneous water oxidation catalysts

Richard I. Sayler, Bryan M. Hunter, Wen Fu, Harry B. Gray, and R. David Britt

J. Am. Chem. Soc., **Just Accepted Manuscript** • DOI: 10.1021/jacs.9b10273 • Publication Date (Web): 31 Dec 2019

Just Accepted

EPR spectroscopy of iron- and nickel-doped [ZnAl]-layered double hydroxides: modeling active sites in heterogeneous water oxidation catalysts

Richard I. Sayler†, Bryan M. Hunter†, Wen Fu†, Harry B. Gray‡, and R. David Britt*†

†Department of Chemistry, University of California at Davis, Davis, California 95616, United States
‡Division of Chemistry and Chemical Engineering, California Institute of Technology, Pasadena, California 91125, United States

Abstract

Iron-doped nickel layered double hydroxides (LDHs) are among the most active heterogeneous water oxidation catalysts. Due to inter-spin interactions, however, the high density of magnetic centers results in line-broadening in magnetic resonance spectra. As a result, gaining atomic-level insight into the catalytic mechanism *via* electron paramagnetic resonance (EPR) is not generally possible. To circumvent spin-spin broadening, iron and nickel atoms were doped into non-magnetic [ZnAl]-LDH materials and the coordination environments of the isolated Fe(III) and Ni(II) sites were characterized. Multifrequency EPR spectroscopy identified two distinct Fe(III) sites (S = 5/2) in [Fe:ZnAl]-LDH. Changes in zero field splitting (ZFS) were induced by dehydration of the material, revealing that one of the Fe(III) sites was solvent-exposed (*i.e.* at an edge, corner, or defect site). These solvent-exposed sites featured an axial ZFS of 0.21 cm^{-1} when hydrated. The ZFS increased dramatically upon dehydration (to -1.5 cm^{-1}), owing to lower symmetry and a decrease in the coordination number of iron. The ZFS of

the other ("inert") Fe(III) site maintained an axial ZFS of 0.19-0.20 cm^{-1} under both hydrated and dehydrated conditions. We observed a similar effect in [Ni:ZnAl]-LDH materials; notably, Ni(II) (S = 1) atoms displayed a single, small ZFS ($\pm$0.30 cm^{-1}) in hydrated material, whereas two distinct Ni(II) ZFS values ($\pm$0.30 and $\pm$1.1 cm^{-1}) were observed in the dehydrated samples. Although the magnetically-dilute materials were not active catalysts, the identification of model sites in which the coordination environments of iron and nickel were particularly labile (*e.g.* by simple vacuum drying) is an important step towards identifying sites in which the coordination number may drop spontaneously in water, a probable mechanism of water oxidation in functional materials.

Introduction

In oxygenic photosynthesis, plants use water as the electron source for storing energy in chemical bonds. In nature, these bonds typically reside in carbohydrates. Lacking the complex protein machinery to functionally mimic plants, we often design systems to store energy in the simplest diatomic covalent bond: dihydrogen (H_2). Regardless of its ultimate form, fuel production relies on water oxidation to generate protons and electrons. Major hurdles in the development of scalable systems for splitting water include the high overpotential needed for the 4-electron/4-proton redox reaction as well as the low rates of catalysis by earth-abundant materials.[1] It is notable that these limitations are present even in rare-element catalysts.

The layered double hydroxide (LDH) (**Figure 1**) structure, which is commonly found in nature (*e.g.* brucite), has been increasingly employed as a robust framework

for water oxidation electrocatalysis.[2,3] The [NiFe]-LDH electrocatalysts [in which some of the nickel(II) sites have been replaced by iron(III)] have been extensively studied in recent years, with iron incorporation playing a critical role in water oxidation activity.[4] Even accidental intercalation of adventitious iron into first-row transition metal LDHs enhances catalytic performance.[5]

In efforts to further improve these heterogeneous catalysts, detailed knowledge of the metal coordination environments is a prerequisite for determining the mechanism by which they operate. A necessary step in the electro-oxidation of water is the liberation of molecular oxygen, generating a low-valent, coordinatively unsaturated metal site which can then weakly bind water or hydroxide. Complicating the issue, not all sites are equivalent in anisotropic nanoparticles or electrodeposited materials, as these structures have bulk, edge, corner, and interstitial sites, each with a different coordination environment.[6–8] In the case of nickel-containing LDH materials, there is little consensus on the mechanism of intercalated iron. While some investigators support the view that surface iron species are the active sites,[9] others propose that the nickel sites are responsible for catalysis.[10]

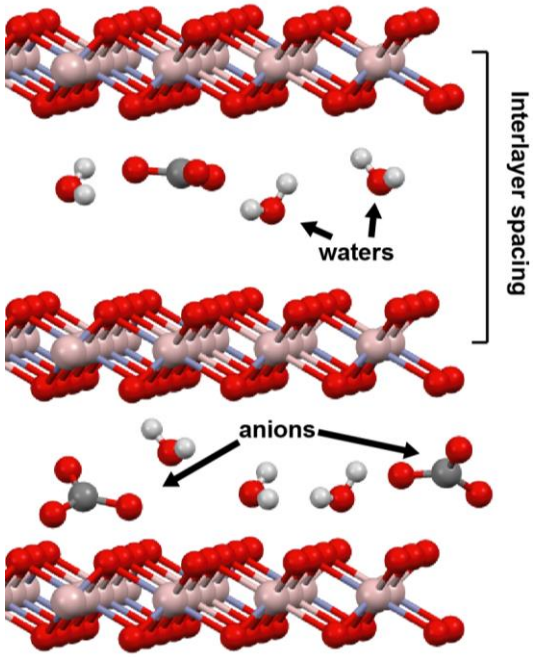

Figure 1. Depiction of an LDH structure with carbonate anions in the interlayer space. Hydroxide hydrogens in the material are omitted for clarity. Oxygen atoms (red), metal atoms (pink), hydrogen atoms (white), and carbon atoms (black).

Recently, Boettcher and coworkers have proposed that the increased activity of Fe-doped NiO_x materials is due to edge Fe sites as opposed to bulk Fe sites.[11] In other first-row transition metal oxides/hydroxides (*e.g.* CoP_i and [NiFe]-LDHs), edges and corners have been identified as most likely to show enhanced catalysis.[6,8,11,12] Additionally, computational studies have suggested that edge iron sites are more active than similar nickel sites in a mixed-metal nickel-iron oxyhydroxide lattice.[7]

In theory, electron paramagnetic resonance (EPR) spectroscopy should be a sensitive indicator of the coordination environment of catalytic metal sites. In practice, however, the X-band continuous wave (CW) EPR spectra of (1) [NiFe]-LDH,[13] (2) electrodeposited Ni(II) in borate[14] (NiB_i, which is structurally similar to LDH),[15] and

coprecipitated FeOOH (goethite)[16] display no signals from isolated metal centers (**Figure 2, 1-3**): Instead, all three materials feature very broad EPR lineshapes (**Figure 2, 1-3**) that result from strong inter-spin electronic couplings between the high density paramagnetic metal centers. Additionally, fast relaxation times make these magnetically dense LDHs unsuitable for pulsed EPR studies, unlike, for example, the Mn-Ca OEC of photosystem II.[17–19] For these reasons, the very limited spectral information we can gather prohibits detailed analysis of individual sites.

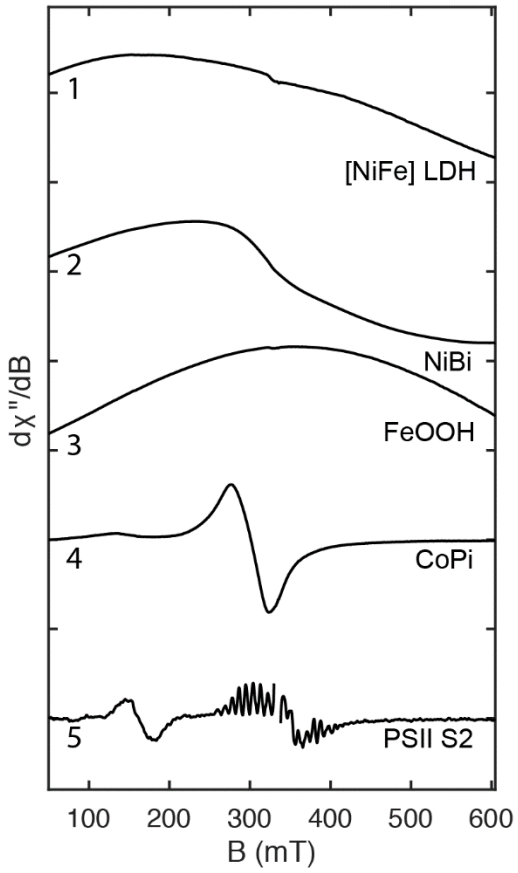

Figure 2. EPR spectra of materials relevant to water oxidation catalysis: (1) 5 mg of [NiFe]-LDH nanopowder synthesized by pulsed laser ablation in liquids (PLAL);[17–19] (2) 5 mg of NiB_i powder synthesized by electrodeposition;[14] (3) 5 mg of FeOOH powder synthesized by coprecipitation;[16] (4) 5 mg of CoP_i synthesized by electrodeposition and subsequent electrochemical oxidation;[20] (5) X-band CW EPR of the S2 state in spinach BBY membranes.[21] Acquisition parameters: (1-3) microwave frequency = 9.4 GHz; temperature = 20 K; microwave power = 2.0 mW; modulation amplitude = 0.5 mT; (4) microwave frequency = 9.4 GHz; temperature = 40 K; microwave power = 2.0 mW; modulation amplitude = 0.5 mT; (5) microwave frequency = 9.4 GHz; temperature = 7 K; microwave power = 200 μW; modulation amplitude = 0.5 mT.

Fortunately EPR spectroscopy has been successfully employed to characterize the coordination environments and electronic structures of paramagnetic centers in a some extended solids with catalytic properties, including anatase (TiO_2),[22] cobalt oxide (CoO_x),[23] zeolites,[24–26] and metal-organic frameworks.[27] A recent example of a well-characterized metal oxide system is the CoP_i catalyst, in which the bulk of the material is low-spin, diamagnetic Co(III). This EPR-silent background allows characterization of relatively well isolated S = 1/2 Co(IV) sites (**Figure 2, 4**).[23] Even in this relatively well-behaved system, pulsed EPR results have not been reported due to relatively fast spin-spin relaxation. Compared to the well-studied S = 1/2 S_2-state of the Mn_4CaO_5 cluster in photosystem II (**Figure 2, 5**),[17–19] relatively little information about the electronic g-values and hyperfine interactions can be gleaned in the absence of data from measurements employing a combination of multifrequency CW spectra supplemented by higher resolution pulsed EPR techniques.[28,29]

In order to mimic the desirable magnetic properties of CoP_i, we doped iron and nickel atoms into a non-magnetic [ZnAl]-LDH material, with the ultimate goal of using EPR spectroscopy to extract the electronic and geometric information of isolated Fe(III) and Ni(II) paramagnetic centers. With the resulting data, we hoped to make comparisons among disparate heterogeneous water oxidation catalysts[13,30] and draw connections to homogeneous models where mechanisms are better understood.[31–33]

Here we report the magnetic parameters of different types of Fe(III) and Ni(II) sites in LDH structures. The primary (aquo/hydroxide) coordination spheres of differentiable Ni(II) and Fe(III) sites were probed using multifrequency CW EPR

spectroscopy following hydration and dehydration cycles. At X-band (9.4 GHz) and Q-band (34 GHz) frequencies, no pulsed EPR signals were observed in either the Fe(III) or Ni(II) doped materials. Interestingly, electron spin echo signals *were* observed for the iron-doped material at D-band (130 GHz). This unexpected finding has opened the way for in-depth investigations of complex LDH high-spin systems by high frequency/high field pulsed EPR.[18,34]

Materials and Methods

Materials synthesis

Dilute LDHs: A solution of 6 mM $Zn(NO_3)_2$ and 2 mM of a variable mixture of $Al(NO_3)_3$ and $Fe(NO_3)_3$ was slowly added (1 mL/min) to a carbonate buffered solution (1 M, pH 10). A cream-colored coprecipitate formed (at higher Fe concentrations the solid was more orange) and the solution was stirred at 50°C for one hour while adjusting the pH with 1M KOH to maintain pH 10. The coprecipitate was filtered and the clay-like solid was dried at 100 °C for one hour. A solution of 2 mM $Al(NO_3)_3$ and 2 mM of a variable mixture of $Zn(NO_3)_2$ and $Ni(NO_3)_2$ was slowly added (1 mL/min) to a carbonate buffered solution (1 M, pH 10). A cream-colored coprecipitate formed (at higher Ni concentrations the solid was more seafoam green) and the solution was stirred at 50°C for one hour while adjusting the pH with 1M KOH to maintain pH 10. The coprecipitate was filtered and the clay-like solid was dried at 100 °C for one hour.

Nickel borate (NiB_i) and cobalt phosphate (CoP_i): thin films were synthesized electrochemically according to literature procedures.[14,20] The films were subsequently scraped off the electrode, packed into an EPR tube, and frozen at 77 K.

[NiFe]-LDH: nanoparticles were synthesized by a pulsed laser ablation in liquids (PLAL) method described previously.[13]

Materials characterization

Syntheses were successful with metal solutions containing M(II) and M(III) ions in a 3:1 ratio.[2] The material phases were confirmed by powder X-ray diffraction (PXRD). Good agreement with literature PXRD patterns for [ZnAl]-LDH indicated the formation of the LDH structure. Slight variations between the [ZnAl]-LDH and [Fe:ZnAl]-LDH patterns were apparent, likely due to changes in the unit cell upon the addition of Fe(III) (**Figure S1**). PXRD data were collected at room temperature using a Bruker D8 ADVANCE Eco at 40 kV and 25 mA. The data were collected in the 5°-70° 2θ range with a step size of 0.0143° and 0.5 s/step. Intensities were normalized (**Figures S1 and S2**).

Electron paramagnetic resonance

X-band CW EPR spectroscopy: EPR samples were prepared either as a dry powder or suspended in 18 MΩ water. X-band continuous-wave (CW) EPR spectra were recorded on a Bruker ELEXSYS E500 spectrometer equipped with a cylindrical TE_{011}-mode resonator (SHQE-W), an ESR 900-liquid helium cryostat, and an ITC-5 temperature controller (Oxford Instruments). Spectra were acquired under slow-passage non-saturating conditions. Background EPR signals from the host [ZnAl]-LDH were differentiated using [ZnAl]-LDH control materials. Oxygen atom radicals and vacancy signals were predictably distinct from observed spectra.

For systems with $S > 1/2$, including high-spin Fe(III) or Ni(II), the spin Hamiltonian was parameterized as in Eqs. 1-3:

$$H_{eff} = H_{ez} + H_{zfs} \quad (1)$$

$$H_{ez} = g\beta m_s B \quad (2)$$

$$H_{zfs} = D[S_z^2 - \frac{1}{3}S^2 + E/D(S_x^2 - S_y^2)] \quad (3)$$

where H_{ez} is the electronic Zeeman energy, H_{zfs} is the zero-field splitting (ZFS) energy, D is the axial contribution to the ZFS, and E is the rhombic contribution to the ZFS. These parameters were used to describe the coordination sphere of the metal center, as splitting only arise when the electronic structure of the metal center is perturbed by ligands. Spin Hamiltonian parameters were determined by numerically simulating multifrequency EPR spectra with the Easy Spin toolbox for MATLAB 5.1.5.[35]

High frequency EPR spectroscopy: All pulsed EPR studies were conducted on a 130 GHz EPR spectrometer[36] equipped with a TE_{011} mode cylindrical resonant cavity designed and manufactured by HF EPR Instruments, Inc. (V. Krymov, New York). The spectrometer features an Oxford-CF935 liquid helium cryostat and an ITC-503 temperature controller. The external magnetic field was generated with an 8 T cryogen-free magnet (Cryogenic Limited, UK). Field-swept echo-detected EPR spectra were acquired using a Hahn echo detection sequence: $\pi/2$-τ-π-τ-echo.

Electrochemical characterization

Linear sweep voltammetry (LSV) and chronoamperometry (CA) were conducted on a Princeton Applied Research (Oak Ridge, TN, USA) Model 263 A potentiostat in a three-electrode system. The reference electrode was an Ag/AgCl (3 M NaCl) electrode (BASi, West Lafayette, IN, USA). The working electrode was prepared by drop-casting 1

cm^2 of a 1 cm x 2 cm fluorine doped tin oxide plate (FTO, Sigma Aldrich Inc., Milwaukee, WI, USA) with 12 μg [Fe:ZnAl]-LDH or [Ni:ZnAl]-LDH from a sonicated suspension in 18 MΩ H_2O. The counter electrode was nickel foam. The electrolyte was 15 mL of 0.5 M sodium phosphate buffer (pH 7 or pH 9). The LSV was taken from the open circuit potential swept to 1.5 V (vs Ag/AgCl) and CA was recorded at an overpotential of ~800 mV. All LSV and CA experiments were conducted with stirring.

Results

The X-band CW EPR signals of NiB_i, FeOOH, and [NiFe]-LDH were found to be broad and featureless at low temperature (**Figure 2, 1-3**), suggesting that each metal center experiences exchange interactions between nearest neighbor sites and dipolar coupling interactions with more distant ions. These interactions give rise to spectral broadening that obscured information about individual paramagnetic centers. Magnetically dilute iron- and nickel-containing [ZnAl]-LDH particles were synthesized to overcome this limitation (*vide supra*).

The X-band spectra of [Fe:ZnAl]-LDH (with 10 - 25% iron) at 20 K featured broad signals similar to those of the low-temperature [NiFe]-LDH material (**Figure 3A, 1 and 2**). At low iron concentrations (1-5% iron), however, the following signals were discernable: (1) a sharp signal at 180 mT; (2) a positive shoulder from 80 to 110 mT; and (3) a negative feature centered at 335 mT (**Figure 3A, 3 and 4**). These spectral features sharpened and decreased in intensity as the iron concentration decreased. To probe the integer spin states of nickel, parallel-mode X-band CW EPR spectra were recorded for [Ni:ZnAl]-LDHs with varying nickel concentration. A negative feature

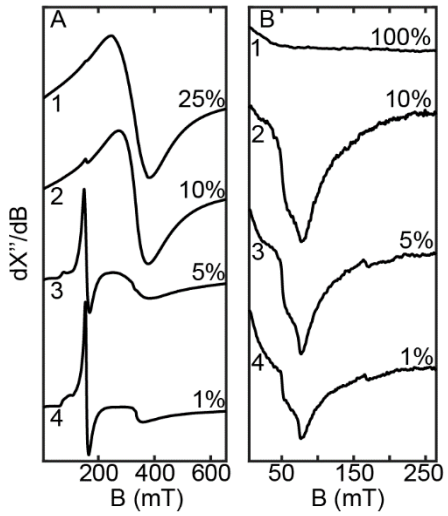

***Figure* 3. A**: Perpendicular-mode EPR spectra of [Fe:ZnAl]-LDH with indicated iron concentrations $[Zn_{0.75}Al_{0.25-x}Fe_x(OH)_2][A]_{0.25}$. **B**: Parallel-mode EPR spectra of [Ni:ZnAl]-LDH with indicated nickel concentrations $[Zn_{0.75-x}Al_{0.25}Ni_x(OH)_2][A]_{0.25}$. Spectra were acquired at 9.4 GHz, 20 K, and 502 μW power. [A] is an arbitrary anion, predominantly carbonate at high pH.

at 80 mT was observed for [Ni:ZnAl]-LDH (with 1-20% nickel); this feature, which was not present in pure NiOOH (**Figure 3B**), sharpened and decreased in intensity as the Ni(II) concentration decreased.

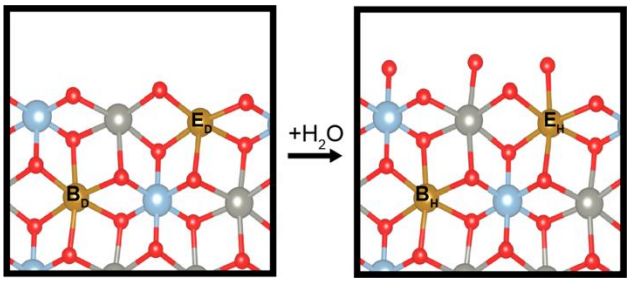

***Figure* 4.** Depiction of edge (E) and interstitial (B) sites under hydrated ($_H$) and dehydrated ($_D$) conditions. Atoms are labeled as follows: orange (iron or nickel), gray (zinc), light blue (aluminum), and red (oxygen).

Based on the structure of LDH materials, we assigned types of Fe and Ni sites in the bulk (B) and in edge, corner, or defect sites (E). These sites were then considered in hydrated ($_H$) (**Figure 4A**) or dehydrated ($_D$) (**Figure 4B**) states. Although dehydrated [Fe(1%):ZnAl]-LDH yielded the CW EPR spectrum shown above (**Figure 5, as synthesized**), several noticeable changes were observed after suspending the sample in water overnight. Upon hydration, the signals at 335 and 110 mT decreased in intensity, while the feature at 40 mT was stronger (**Figure 5, hydrated**). No changes were observed in the intensities at 80 and 180 mT. These changes were reversible over several hydration-dehydration cycles (**Figure 5, hydrated, dehydrated**). Spectral features also were highly dependent on water being the solvent; no changes were observed when the dehydrated sample was subsequently treated with acetonitrile.

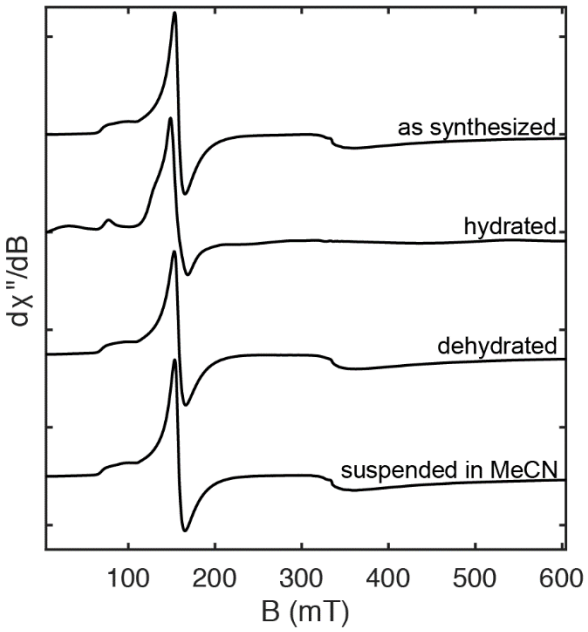

Figure 5. EPR spectra of [Fe:ZnAl]-LDH (with 1% iron) under different solvation conditions, as indicated. Spectra were acquired at 9.4 GHz and 502 μW microwave power.

The spectra for [Fe:ZnAl]-LDH were best simulated with two types of $S = 5/2$ sites. In the absence of pulsed EPR experiments, determination of accurate magnetic parameters is very challenging. Fortuitously, the [Fe:ZnAl]-LDH (with 1% iron) gave an observable electron spin echo at 130 GHz and 10 K (**Figure 6C and 6D**), a rare example of echo-detected high-spin Fe(III) centers. Subsequent high-frequency pulsed echo experiments allowed us to simulate spectra at multiple frequencies, providing an accurate determination of D and E parameters.

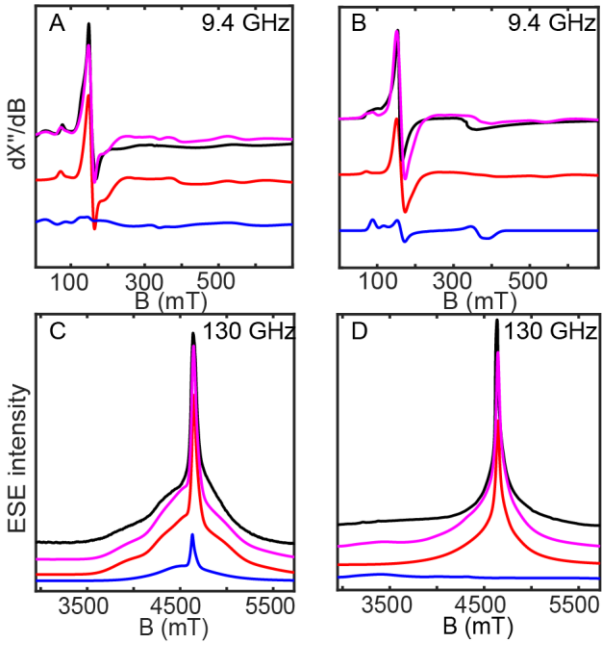

Figure 6. CW and pulsed spin echo spectra of hydrated [Fe:ZnAl]-LDH (left) and dehydrated [Fe:ZnAl]-LDH (right). Panels **A and B** at 9.4 GHz (30 K); panels **C and D** at 130 GHz (7 K). Simulation parameters: class B_H (red, panels **A and C**) S = 5/2, *g* = 2.003, D = 0.20 cm^{-1}, E = 0.044 cm^{-1}; class B_D (red, panels **B and D**) S = 5/2, *g* = 2.003, D = 0.19 cm^{-1}, E = 0.050 cm^{-1}; class E_H (blue, panels **A and C**) S = 5/2, *g* = 2.003, D = 0.21 cm^{-1}, E = 0.020 cm^{-1}; class E_D (blue, panels **A and C**) S = 5/2, *g* = 2.003, D = -1.5 cm^{-1}, E = 0.32 cm^{-1}. The sum of the components is in magenta.

The multifrequency spectra were fitted, yielding ZFS magnetic parameters of the various types of iron sites. The self-consistent ZF splittings for B_H(Fe) and B_D(Fe) were simulated with *g* = 2.003 (both), and *D* = 0.20 cm^{-1} and 0.19 cm^{-1} and *E* = 0.044 cm^{-1} and 0.050 cm^{-1}, respectively, at 130 and 9.4 GHz (**Figure 6**). The ZF splittings of E_H(Fe) and E_D(Fe) were simulated with *D* = 0.21 and -1.5 cm^{-1}, *E* = 0.020 and 0.32 cm^{-1}, respectively, at 130 and 9.4 GHz. Echo intensity for E_D(Fe) was observed down to 3000

mT at 130 GHz, (**Figure 6D**); this was not the case for the hydrated material [E_H(Fe)] where the features were considerably narrower (**Figure 6C**). The assignments of multiple species also were tracked by observing the changes in spectral intensity as a function of temperature (see SI).

Spectra of nickel-containing LDHs exhibited similar structural changes upon hydration and dehydration. The X-band parallel-mode derivative spectrum of the initially dehydrated [Ni:ZnAl]-LDH (with 1% nickel) featured a negative region centered at 80 mT and a minor positive signal at 160 mT (**Figure 7B**). Upon hydration, the signal at 160 mT was no longer observed, and the signal at 80 mT was unchanged (**Figure 7A**). Further heating under vacuum (150°C) resulted in increased intensity of the 160 mT component.

The X-band parallel mode spectra of hydrated [Ni:ZnAl]-LDH were well-simulated by one type of S = 1 site. Specifically, B_H(Ni) = E_H(Ni): g = [2.3 2.2 2.2], D = ±0.32 cm^{-1}, and E = 0.050 cm^{-1} (**Figure 7A**). Simulation of dehydrated [Ni:ZnAl]-LDH required two different types of S = 1 sites, with the following magnetic parameters: B_D(Ni): g = [2.3 2.2 2], D = ±0.30, and cm^{-1} E = 0.050 cm^{-1}; E_D(Ni): g = [2.3 2.2 2], D = ±1.1 cm^{-1}, and E = 0.030 cm^{-1} (**Figure 7B**). The relatively small ZFS associated with Ni(II) sites made it possible to observe the “EPR-silent” (S = 1) Ni(II) via parallel-mode EPR.[37]

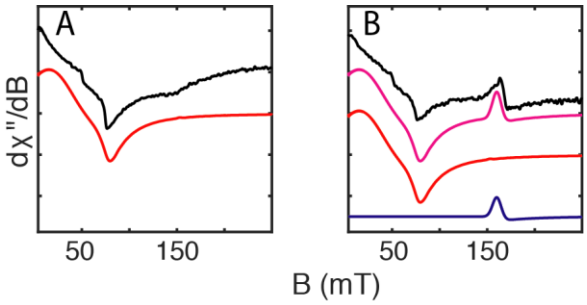

Figure 7. Parallel-mode CW EPR spectra of **A**: hydrated [Ni:ZnAl]-LDH (with 1% nickel) and **B**: dehydrated [Ni:ZnAl]-LDH (with 1% nickel). Spectra acquired at 9.4 GHz, 5 K and 3.2 mW power. Simulations parameters: B_D, B_H, and E_H (red, panels **A and B**): S = 1, g = [2.3 2.2 2.2], D = ±0.30 cm^{-1} , E = 0.050 cm^{-1}; E_D (blue, panel **B**): S = 1, g = [2.3 2.2 2], D = ±1.1 cm^{-1}, E = 0.030 cm^{-1}. The sum of the components is in magenta.

Ni(III), Fe(IV), Fe(V) and Fe(VI) have all been implicated in the water oxidation mechanisms in the related NiFE LDH.[9] The ability to monitor the oxidation state of the isolated Fe and Ni sites of [Fe:ZnAl]- LDH and [Ni:ZnAl]- LDH via EPR is of great interest in isolating mechanistically relevant higher oxidation state sites in these materials. Attempts to oxidize both [Fe:ZnAl]- LDH and [Ni:ZnAl]- LDH were made with a variety of chemical oxidants, including in both aqueous and non-aqueous solvents, though no new species could be attributed to oxidized Fe or Ni species. The complex chemical environment of these materials include water, hydroxide and anions such as carbonate and nitrate, which are known to react with high oxidation state Fe and/or Ni centers in these materials which could cause the rapid decay of high oxidation state intermediates.

The electrochemical properties of [Fe:ZnAl]-LDH and [Ni:ZnAl]-LDH were tested at pH 7 and pH 9 in potassium phosphate buffer. Linear sweep voltammetry and

constant-potential chronoamperometry were conducted on a thin film of material made by drop casting 50 μL of a 5 mg/mL suspension of materials onto a glassy carbon working electrode. These materials were found to anodically shift the onset potential of water oxidation relative to the bare electrode, likely due to the insulating quality of the dilute materials (**Figure S8-S11**). The chronoamperometric current also decreased relative to the bare electrode at doping levels of < 5% Fe or Ni (**Figure S8-S11**). It is concluded that, while these materials are excellent structural models for active OER catalysts, they are not in themselves active.

Discussion

The broad, featureless EPR signals characteristic of NiB_i, FeOOH, and [NiFe]-LDH at low temperatures are indicative of highly-coupled metal oxide particles each with a high density of paramagnetic sites. This spectral broadening limits the information obtainable by EPR spectroscopy, in particular the coordination environments of individual paramagnets.

Magnetically dilute model materials are able to overcome these limitations, and the features observed in 1-5% [Fe:ZnAl]-LDH are signatures of isolated, high-spin Fe(III).[38] In addition, parallel-mode CW EPR can probe integer spin states [as in Ni(II)], owing to mixing of microstates that causes relaxation of EPR selection rules.[39] As a result, both [Fe:ZnAl]-LDH and [Ni:ZnAl]-LDH exhibited spectral features indicative of isolated paramagnetic centers.

By coupling low frequency CW EPR with high-frequency echo-detected EPR, two types of sites were identified in 1% [Fe:ZnAl]-LDH. The two bulk-site types, present

under different hydration conditions, B(Fe), were well-simulated using virtually identical ZF splitting parameters (**Table 1**).

	Bulk Class (B)	**Edge Class (E)**
Dehydrated (D)	**Fe** D: 0.19 cm^{-1} [a,b] E: 0.050 cm^{-1} [a,b]	**Fe** D: -1.5 cm^{-1} [a,b,d] E: 0.32 cm^{-1} [a,b]
	Ni D: ±0.30 cm^{-1} [c] E: 0.050 cm^{-1} [c]	**Ni** D: ±1.1 cm^{-1} [c] E: 0.030 cm^{-1} [c]
Hydrated (H)	**Fe** D: 0.20 cm^{-1} [a,b,d] E: 0.044 cm^{-1} [a,b]	**Fe** D: 0.21 cm^{-1} [a,b,d] E: 0.020 cm^{-1} [a,b]
	Ni D: ±0.30 cm^{-1} [c] E: 0.050 cm^{-1} [c]	**Ni** D: ±0.30 cm^{-1} [c] E: 0.050 cm^{-1} [c]

Table 1. ZF splitting parameters for isolated Fe(III) and Ni(II) sites in a magnetically dilute LDH material. [a] Determined from CW X-band simulation; [b] Determined from pulsed D-band simulation; [c] Determined from parallel-mode CW X-band simulation; [d] Determined from CW X-band temperature dependence (Supporting Information section II).

Because only slight changes in ZF splitting were observed under both hydrated and dehydrated conditions, the iron sites likely are “locked” within the lattice. These sites, which contain triply bridging hydroxide ligands, will not be labile (**Figure 4**).

The assigned edge sites, E(Fe), required very different ZF splitting parameters for simulations of hydrated *vs.* dehydrated materials (**Table 1**). The dramatic increase in ZF splittings indicates that the coordination environments of these metal centers are undergoing substantial changes. These edge, corner, and defect sites must be coordinated by labile waters or hydroxides, and ligand losses likely will occur upon

heating.[40,41,39] Five-coordinate (square pyramidal and trigonal bipyramidal) high-spin Fe(III) systems have ZF splittings similar to those of dehydrated sites (**Table 2**). When hydrated, both types of Fe sites (edge and interstitial) are coordinated by a full octahedral ligand set, with either μ_3-oxo bonds or terminal waters and hydroxides. The highly symmetric coordination environment, along with Fe-O bond covalency, gave rise to small ZF splittings[42] in B_H(Fe), B_D(Fe), and E_H(Fe). The extremely broad spectrum seen in the high-frequency echo-detected spectrum was expected, as the microwave excitation energy is of similar magnitude to the axial ZFS parameter (D = -1.5 cm^{-1}, f_{mw} = 4.3 cm^{-1}).

Similar site-specific assignments have been made in Fe-doped zeolites.[43] In zeolite systems, a characteristic g = 2 signal is observed and assigned to iron dimers.[44] In the present system, as we see no similar feature, we conclude that the iron sites in these dilute, functional materials are not aggregated. The ZFS parameters used to fit the spectra of [Fe:ZnAl]-LDH are set out in **Table 1**, alongside those of model complexes with varying coordination geometries.

As in the iron case, two types of nickel sites were identifiable in 1%-[Ni:ZnAl]-LDH utilizing parallel-mode EPR. B_D(Ni) and E_D(Ni) had significant differences in splittings, with very similar g-tensors, as expected for B(Ni) sites arising from bulk or inter-lattice Ni(II) in an octahedral ligand field (**Figure 4**). Furthermore, E(Ni) likely is an edge or defect Ni(II) site that changes coordination number and geometry under different hydration conditions. In the hydrated material, the spectrum was simulated using a single ensemble with the same ZF splitting parameters. B_D, B_H, and E_H all

exhibited ZF splittings similar to that of $Ni(en)_3^{2+}$ doped into $Zn(en)_3(NO_3)_2$ and Ni(II) doped into $ZnSiF_6 \bullet 6H_2O$, both of which are 6-coordinate and octahedral.[45,46]

High-valent metal sites, such as Ni(III), Fe(IV), Fe(V) and Fe(VI) have been suggested in the water oxidation mechanisms in the related [NiFe]-LDH.[9] The ability to monitor the oxidation state of the isolated Fe and Ni sites of [Fe:ZnAl]-LDH and [Ni:ZnAl]-LDH *via* EPR would be of great interest in this ongoing conversation. Attempts were made to oxidize both [Fe:ZnAl]-LDH and [Ni:ZnAl]-LDH with a number of chemical oxidants, both in aqueous and non-aqueous solvents. No spectral changes could unequivocally be attributed to oxidized Fe or Ni species. The spectroscopic features reported here provide a basis for further study of edge-site oxidation states.

Furthermore, although these materials feature Fe(III)/Ni(II) sites, the catalytic resting states of the functional catalysts are almost certainly Fe(III)/Ni(III). In this oxidized form, the iron centers would likely lose ligands before nickel, since Ni(III) would be substantially less labile than Ni(II). Thus, if ligand loss is an early step in catalysis, our analysis implicates iron.

Species	Ligand sphere	Ligand geometry	D (cm^{-1})	E(cm^{-1})	g_{iso}	citation
Fe(III)						
Class B_H	O_6	O_h	0.20	0.044	2.003	This work
Class B_D	O_6	O_h	0.19	0.050	2.003	This work
Class E_H	O_6	O_h	0.21	0.020	2.003	This work
Class E_D	O_5	Not O_h	-1.5	0.32	2.003	This work
Fe(III) in $PdTiO_3$	O_6	O_h	1.176	0	2.002	[42]
Fe(III) in Al_2O_3	O_6	O_h	0.1683	0.00159	2.003	[42]
Fe(III) citrate pH 2	O_6	O_h	-0.12	0	2.004	[47]
Fe(III) citrate pH 6	O_6	O_h	0.024	0.008	2	[47]
$[Fe(catecholate)_3]^{3-}$	O_6	O_h	0.319	0.023	2	[48]
Fe(III)-EDTA	N_2O_4	O_h	-0.77	-0.21	2.004	[49]
Fe(III)-transferrin (Human)	NO_5	O_h	0 .42	0.11		[50]
Met-Hemoglobin	N_4O	Sq. pyramidal	10.7	0	1.95	[51]
Met-Myoglobin	N_4O	Sq. pyramidal	9-9.5	0	1.98	[51]
Ni(II)						
Class B_H,E_H	O_6		$\pm$0.30	0.050	2.2	This work
Class B_D	O_6		$\pm$0.30	0.050	2.2	This work
Class E_D	O_5		$\pm$1.1	0.030	2.2	This work
$(Zn,Ni)SiF_6 \cdot 6H_2O$	O_6		-0.6	0	2.26	[46]
Ni in $Zn(en)_3$	O_6		0.832	0	2.16	[45]
Ni(*i*Prtacn)	N_3Cl_2		15	0.19	2.06	[52]

Table 2. Comparison of ZF splitting parameters of isolated Fe(III) an Ni(II) centers in different coordination environments.

Conclusions

The identification and characterization of isolated Fe(III) and Ni(II) centers in LDH-structured materials contribute to the ongoing discussion of their catalytic mechanisms. Ultimately, we aim to answer the question of which sites are active for electrocatalytic water splitting. Here, we find that iron and nickel at edge sites readily

lose water and hydroxide ligands under gentle vacuum heating, revealing a possible mechanism by which high-valent metal-oxo units responsible for catalysis can be generated. However, the same speciation has been identified in both [Ni:ZnAl]-LDH and [Fe:ZnAl]-LDH, suggesting that iron and nickel sites can undergo similar geometric changes.

The structural changes seen at edge, corner, and defect sites are critically important for activity if the mechanism is hydroxide or water attack on a metal-oxo unit. To promote oxo attack by a nucleophile, there must be exceptionally strong metal-oxo π-bonding.[53,54] Such bonding is not possible for lower-valent metals, as one or more of their *d* electrons will be forced to occupy metal-oxo π^* orbitals. But with coordinatively unsaturated sites, multiple bonds to oxos can exist in lower oxidation states of iron.

Associated Content

Supporting Information

ICP-MS of synthesized materials, powder XRD of synthesized materials, calculation of zfs parameters, electrochemical characterization (CV/LSV), supporting figures and tables. This material is available free of charge via the Internet at http://pubs.acs.org.

Author Information

Corresponding Authors

rdbritt@ucdavis.edu

Acknowledgments

This work was supported by the NSF CCI Solar Fuels Program (CHE-1305124) and the Arnold and Mabel Beckman Foundation.

References

(1) Gray, H. B. Powering the Planet with Solar Fuel. *Nat. Chem.* **2009**, *1*, 7.

(2) Anantharaj, S.; Karthick, K.; Kundu, S. Evolution of Layered Double Hydroxides (LDH) as High Performance Water Oxidation Electrocatalysts: A Review with Insights on Structure, Activity and Mechanism. *Mater. Today Energy* **2017**, *6*, 1–26.

(3) Hunter, B. M.; Gray, H. B.; Müller, A. M. Earth-Abundant Heterogeneous Water Oxidation Catalysts. *Chem. Rev.* **2016**, *116*, 14120–14136.

(4) Hunter, B. M.; Winkler, J. R.; Gray, H. B. Iron Is the Active Site in Nickel/Iron Water Oxidation Electrocatalysts. *Molecules* **2018**, *23*, 903.

(5) Trotochaud, L.; Young, S. L.; Ranney, J. K.; Boettcher, S. W. Nickel–Iron Oxyhydroxide Oxygen-Evolution Electrocatalysts: The Role of Intentional and Incidental Iron Incorporation. *J. Am. Chem. Soc.* **2014**, *136*, 6744–6753.

(6) Ullman, A. M.; Brodsky, C. N.; Li, N.; Zheng, S.-L.; Nocera, D. G. Probing Edge Site Reactivity of Oxidic Cobalt Water Oxidation Catalysts. *J. Am. Chem. Soc.* **2016**, *138*, 4229–4236.

(7) Friebel, D.; Louie, M. W.; Bajdich, M.; Sanwald, K. E.; Cai, Y.; Wise, A. M.; Cheng, M.-J.; Sokaras, D.; Weng, T.-C.; Alonso-Mori, R.; Davis, R. C.; Bargar, J. R.; Nørskov, J. K.; Nilsson, A.; Bell, A. T. Identification of Highly Active Fe Sites in (Ni,Fe)OOH for Electrocatalytic Water Splitting. *J. Am. Chem. Soc.* **2015**, *137*, 1305–1313.

(8) Hunter, B. M.; Hieringer, W.; Winkler, J. R.; Gray, H. B.; Müller, A. M. Effect of Interlayer Anions on [NiFe]-LDH Nanosheet Water Oxidation Activity. *Energy Environ. Sci.* **2016**, *9*, 1734–1743.

(9) Hunter, B. M.; Thompson, N. B.; Müller, A. M.; Rossman, G. R.; Hill, M. G.; Winkler, J. R.; Gray, H. B. Trapping an Iron(VI) Water-Splitting Intermediate in Nonaqueous Media. *Joule* **2018**, *2*, 747–763.

(10) Li, N.; Bediako, D. K.; Hadt, R. G.; Hayes, D.; Kempa, T. J.; von Cube, F.; Bell, D. C.; Chen, L. X.; Nocera, D. G. Influence of Iron Doping on Tetravalent Nickel Content in Catalytic Oxygen Evolving Films. *Proc. Natl. Acad. Sci.* **2017**, *114*, 1486.

(11) Stevens, M. B.; Trang, C. D. M.; Enman, L. J.; Deng, J.; Boettcher, S. W. Reactive Fe-Sites in Ni/Fe (Oxy)Hydroxide Are Responsible for Exceptional Oxygen Electrocatalysis Activity. *J. Am. Chem. Soc.* **2017**, *139*, 11361–11364.

(12) Song, F.; Hu, X. Exfoliation of Layered Double Hydroxides for Enhanced Oxygen Evolution Catalysis. *Nat. Commun.* **2014**, *5*, 4477.

(13) Hunter, B. M.; Blakemore, J. D.; Deimund, M.; Gray, H. B.; Winkler, J. R.; Müller, A. M. Highly Active Mixed-Metal Nanosheet Water Oxidation Catalysts Made by Pulsed-Laser Ablation in Liquids. *J. Am. Chem. Soc.* **2014**, *136*, 13118–13121.

(14) Dincă, M.; Surendranath, Y.; Nocera, D. G. Nickel-Borate Oxygen-Evolving Catalyst That Functions under Benign Conditions. *Proc. Natl. Acad. Sci.* **2010**, *107*, 10337.

(15) Bediako, D. K.; Lassalle-Kaiser, B.; Surendranath, Y.; Yano, J.; Yachandra, V. K.; Nocera, D. G. Structure–Activity Correlations in a Nickel–Borate Oxygen Evolution Catalyst. *J. Am. Chem. Soc.* **2012**, *134*, 6801–6809.

(16) Ruby, C.; Usman, M.; Naille, S.; Hanna, K.; Carteret, C.; Mullet, M.; François, M.; Abdelmoula, M. Synthesis and Transformation of Iron-Based Layered Double Hydroxides. *Synth. Clay-Based Mater. Layer. Double Hydroxides* **2010**, *48*, 195–202.
(17) Cox, N.; Pantazis, D. A.; Neese, F.; Lubitz, W. Biological Water Oxidation. *Acc. Chem. Res.* **2013**, *46*, 1588–1596.
(18) Cox, N.; Retegan, M.; Neese, F.; Pantazis, D. A.; Boussac, A.; Lubitz, W. Electronic Structure of the Oxygen-Evolving Complex in Photosystem II Prior to O-O Bond Formation. *Science* **2014**, *345*, 804.
(19) Oyala, P. H.; Stich, T. A.; Debus, R. J.; Britt, R. D. Ammonia Binds to the Dangler Manganese of the Photosystem II Oxygen-Evolving Complex. *J. Am. Chem. Soc.* **2015**, *137*, 8829–8837.
(20) Kanan, M. W.; Nocera, D. G. In Situ Formation of an Oxygen-Evolving Catalyst in Neutral Water Containing Phosphate and Co^{2+}. *Science* **2008**, *321* (5892), 1072.
(21) Marchiori, D. A.; Oyala, P. H.; Debus, R. J.; Stich, T. A.; Britt, R. D. Structural Effects of Ammonia Binding to the Mn_4CaO_5 Cluster of Photosystem II. *J. Phys. Chem. B* **2018**, *122*, 1588–1599.
(22) Howe, R. F.; Gratzel, Michael. EPR Study of Hydrated Anatase under UV Irradiation. *J. Phys. Chem.* **1987**, *91*, 3906–3909.
(23) McAlpin, J. G.; Surendranath, Y.; Dincă, M.; Stich, T. A.; Stoian, S. A.; Casey, W. H.; Nocera, D. G.; Britt, R. D. EPR Evidence for Co(IV) Species Produced During Water Oxidation at Neutral PH. *J. Am. Chem. Soc.* **2010**, *132*, 6882–6883.
(24) Goldfarb, D.; Strohmaier, K. G.; Vaughan, D. E. W.; Thomann, H.; Poluektov, O. G.; Schmidt, J. Studies of Framework Iron in Zeolites by Pulsed ENDOR at 95 GHz. *J. Am. Chem. Soc.* **1996**, *118*, 4665–4671.
(25) Baute, D.; Arieli, D.; Neese, F.; Zimmermann, H.; Weckhuysen, B. M.; Goldfarb, D. Carboxylate Binding in Copper Histidine Complexes in Solution and in Zeolite Y: X- and W-Band Pulsed EPR/ENDOR Combined with DFT Calculations. *J. Am. Chem. Soc.* **2004**, *126*, 11733–11745.
(26) Pietrzyk, P.; Podolska, K.; Mazur, T.; Sojka, Z. Heterogeneous Binding of Dioxygen: EPR and DFT Evidence for Side-On Nickel(II)–Superoxo Adduct with Unprecedented Magnetic Structure Hosted in MFI Zeolite. *J. Am. Chem. Soc.* **2011**, *133*, 19931–19943.
(27) Brozek, C. K.; Dincă, M. Ti^{3+}-, $V^{2+/3+}$-, $Cr^{2+/3+}$-, Mn^{2+}-, and Fe^{2+}-Substituted MOF-5 and Redox Reactivity in Cr- and Fe-MOF-5. *J. Am. Chem. Soc.* **2013**, *135*, 12886–12891.
(28) Peloquin, J. M.; Campbell, K. A.; Randall, D. W.; Evanchik, M. A.; Pecoraro, V. L.; Armstrong, W. H.; Britt, R. D. 55Mn ENDOR of the S2-State Multiline EPR Signal of Photosystem II: Implications on the Structure of the Tetranuclear Mn Cluster. *J. Am. Chem. Soc.* **2000**, *122*, 10926–10942.
(29) Kim, D. H.; Britt, R. D.; Klein, M. P.; Sauer, K. The Manganese Site of the Photosynthetic Oxygen-Evolving Complex Probed by EPR Spectroscopy of Oriented Photosystem II Membranes: The g = 4 and g = 2 Multiline Signals. *Biochemistry* **1992**, *31*, 541–547.
(30) Jung, S.; McCrory, C. C. L.; Ferrer, I. M.; Peters, J. C.; Jaramillo, T. F. Benchmarking Nanoparticulate Metal Oxide Electrocatalysts for the Alkaline Water Oxidation Reaction. *J. Mater. Chem. A* **2016**, *4*, 3068–3076.
(31) Oloo, W. N.; Que, L. Bioinspired Nonheme Iron Catalysts for C–H and C═C Bond Oxidation: Insights into the Nature of the Metal-Based Oxidants. *Acc. Chem. Res.* **2015**, *48*, 2612–2621.

(32) Codolà, Z.; Gómez, L.; Kleespies, S. T.; Que Jr, L.; Costas, M.; Lloret-Fillol, J. Evidence for an Oxygen Evolving Iron–Oxo–Cerium Intermediate in Iron-Catalysed Water Oxidation. *Nat. Commun.* **2015**, *6*, 5865.

(33) Gersten, S. W.; Samuels, G. J.; Meyer, T. J. Catalytic Oxidation of Water by an Oxo-Bridged Ruthenium Dimer. *J. Am. Chem. Soc.* **1982**, *104*, 4029–4030.

(34) Nguyen, A. I.; Suess, D. L. M.; Darago, L. E.; Oyala, P. H.; Levine, D. S.; Ziegler, M. S.; Britt, R. D.; Tilley, T. D. Manganese–Cobalt Oxido Cubanes Relevant to Manganese-Doped Water Oxidation Catalysts. *J. Am. Chem. Soc.* **2017**, *139*, 5579–5587.

(35) Stoll, S.; Schweiger, A. EasySpin, a Comprehensive Software Package for Spectral Simulation and Analysis in EPR. *J. Magn. Reson.* **2006**, *178*, 42–55.

(36) Oyala, P. H.; Ravichandran, K. R.; Funk, M. A.; Stucky, P. A.; Stich, T. A.; Drennan, C. L.; Britt, R. D.; Stubbe, J. Biophysical Characterization of Fluorotyrosine Probes Site-Specifically Incorporated into Enzymes: E. Coli Ribonucleotide Reductase As an Example. *J. Am. Chem. Soc.* **2016**, *138*, 7951–7964.

(37) Krzystek, J.; Park, J.-H.; Meisel, M. W.; Hitchman, M. A.; Stratemeier, H.; Brunel, L.-C.; Telser, J. EPR Spectra from "EPR-Silent" Species: High-Frequency and High-Field EPR Spectroscopy of Pseudotetrahedral Complexes of Nickel(II). *Inorg. Chem.* **2002**, *41*, 4478–4487.

(38) Aasa, R.; Vänngård, tore. EPR Signal Intensity and Powder Shapes: A Reexamination. *J. Magn. Reson. 1969* **1975**, *19*, 308–315.

(39) Campbell, K. A.; Lashley, M. R.; Wyatt, J. K.; Nantz, M. H.; Britt, R. D. Dual-Mode EPR Study of Mn(III) Salen and the Mn(III) Salen-Catalyzed Epoxidation of Cis-β-Methylstyrene. *J. Am. Chem. Soc.* **2001**, *123*, 5710–5719.

(40) Williams, R. J. P. Biological Magnetic Resonance, Vol. 1, Plenum Press, New York and London, **1978**.

(41) Wright, C. M. R.; Ruengkajorn, K.; Kilpatrick, A. F. R.; Buffet, J.-C.; O'Hare, D. Controlling the Surface Hydroxyl Concentration by Thermal Treatment of Layered Double Hydroxides. *Inorg. Chem.* **2017**, *56*, 7842–7850.

(42) Krzystek, J.; Ozarowski, A.; Telser, J. Multi-Frequency, High-Field EPR as a Powerful Tool to Accurately Determine Zero-Field Splitting in High-Spin Transition Metal Coordination Complexes. *20th Int. Conf. Coord. Bioinorg. Chem.* **2006**, *250*, 2308–2324.

(43) Goldfarb, D.; Bernardo, M.; G. Strohmaier, K.; Vaughan, D.; Thomann, H. Characterization of Iron in Zeolites by X-Band and Q-Band ESR, Pulsed ESR, and UV-Visible Spectroscopies. *J. Am. Chem. Soc.* **1994**,116, 6344–6353.

(44) Osadchii, D. Y.; Olivos-Suarez, A. I.; Szécsényi, Á.; Li, G.; Nasalevich, M. A.; Dugulan, I. A.; Crespo, P. S.; Hensen, E. J. M.; Veber, S. L.; Fedin, M. V.; Sankar, G.; Pidko, E. A.; Gascon, J. Isolated Fe Sites in Metal Organic Frameworks Catalyze the Direct Conversion of Methane to Methanol. *ACS Catal.* **2018**, *8*, 5542–5548.

(45) Sreeramachandra Prasad, L.; Subramanian, S. Zero Field Tensor for Ni(II) in Zn (Ethylenediamine)$_3$ (NO_3)$_2$: EPR Study. *J. Chem. Phys.* **1988**, *88*, 43–45.

(46) Shrivastava, K. N.; Rubins, R. S.; Hutton, S.; Drumheller, J. E. Temperature Dependence of the g Value of Ni^{2+} in ZnSiF6·6H2O. *J. Chem. Phys.* **1988**, *88*, 705–706.

(47) Biaso, F.; Duboc, C.; Barbara, B.; Serratrice, G.; Thomas, F.; Charapoff, D.; Béguin, C. High-Field EPR Study of Frozen Aqueous Solutions of Iron(III) Citrate Complexes. *Eur. J. Inorg. Chem.* **2005**, *2005*, 467–478.

(48) Weisser, J. T.; Nilges, M. J.; Sever, M. J.; Wilker, J. J. EPR Investigation and Spectral Simulations of Iron−Catecholate Complexes and Iron−Peptide Models of Marine Adhesive Cross-Links. *Inorg. Chem.* **2006**, *45*, 7736–7747.

(49) Mathies, G.; Blok, H.; Disselhorst, J. A. J. M.; Gast, P.; van der Meer, H.; Miedema, D. M.; Almeida, R. M.; Moura, J. J. G.; Hagen, W. R.; Groenen, E. J. J. Continuous-Wave EPR at 275GHz: Application to High-Spin Fe^{3+} Systems. *J. Magn. Reson.* **2011**, *210*, 126–132.

(50) Mathies, G.; Gast, P.; Chasteen, N. D.; Luck, A. N.; Mason, A. B.; Groenen, E. J. J. Exploring the Fe(III) Binding Sites of Human Serum Transferrin with EPR at 275 GHz. *JBIC J. Biol. Inorg. Chem.* **2015**, *20*, 487–496.

(51) Nehrkorn, J.; Martins, B. M.; Holldack, K.; Stoll, S.; Dobbek, H.; Bittl, R.; Schnegg, A. Zero-Field Splittings in MetHb and MetMb with Aquo and Fluoro Ligands: A FD-FT THz-EPR Study. *Mol. Phys.* **2013**, *111*, 2696–2707.

(52) Rebilly, J.-N.; Charron, G.; Rivière, E.; Guillot, R.; Barra, A.-L.; Serrano, M. D.; van Slageren, J.; Mallah, T. Large Magnetic Anisotropy in Pentacoordinate Ni^{II} Complexes. *Chem. Eur. J.* **2008**, *14*, 1169–1177.

(53) Winkler, J. R.; Gray, H. B. Electronic Structures of Oxo-Metal Ions. In *Molecular Electronic Structures of Transition Metal Complexes I*; Mingos, D. M. P., Day, P., Dahl, J. P., Eds.; Springer Berlin Heidelberg: Berlin, Heidelberg, 2012; pp 17–28.

(54) Gray, H. B.; Winkler, J. R. Living with Oxygen. *Acc. Chem. Res.* **2018**, *51*, 1850–1857.

Table of Contents Graphic